NJC

ROYAL SOCIETY OF CHEMISTRY

PAPER

View Article Online
View Journal | View Issue

Check for updates

Cite this: *New J. Chem.*, 2025, **49**, 3067

Structural and thermal properties of 3-substituted quinazolinone Schiff base conjugates†

Milenko Korica,[a] Mario Komar,[b] Maja Molnar,[b] Vinko Nemec,[c] Dominik Cinčić[c] and Tomislav Balić*[a]

Quinazolinone Schiff base conjugates have recently attracted considerable attention from the scientific community due to their potential application as anti-cancer drugs and promising multidentate ligands. Unfortunately, reports dealing with the structural characterization of these compounds are incomprehensibly scarce. To explore the supramolecular features of these perspective compounds we have prepared and crystallized four quinazolinone Schiff base conjugates (**1** = 3-{(*E*)-[(2-chlorophenyl)methylidene]amino}-2-methylquinazolin-4(3*H*)-one, **2** = 3-{(*E*)-[(2,4-dihydroxyphenyl)methylidene]amino}-2-methylquinazolin-4(3*H*)-one, **3** = 3-{(*E*)-[(2,3-dihydroxyphenyl)methylidene]amino}-2-methylquinazolin-4(3*H*)-one and **4** = 3-[(*E*)-benzylideneamino]-2-methylquinazolin-4(3*H*)-one). Single crystals were obtained by recrystallization of crude products from different solvents, and crystal structures were determined by single crystal X-ray diffraction. Considering their molecular structure, these compounds are similar, with the most pronounced difference being the dihedral angle between the two aromatic systems. In the crystal state, compounds with –OH groups on the benzene ring (**2** and **3**) are primarily connected by strong O–H···N hydrogen bonds, and unsubstituted (**4**) and Cl-substituted (**1**) compounds *via* N–H···O and C–H···O hydrogen bonds. Thermal analysis results have shown that among these compounds the 2,4-OH substituted **2** (226 °C) has the highest melting point, followed by 2,3-OH substituted **3** (201 °C), unsubstituted **4** (192 °C), and the Cl-substituted **1** (159 °C). Additional Hirshfeld surface analysis and intermolecular energy calculations indicate that hydrogen bonds have the largest impact on thermal stability and that dispersive interactions are important for stability, but can be sterically hindered by bulky substituents on aromatic systems.

Received 13th September 2024,
Accepted 17th January 2025

DOI: 10.1039/d4nj04028g

rsc.li/njc

Open Access Article. Published on 21 January 2025. Downloaded on 2/13/2026 11:23:58 AM.
This article is licensed under a Creative Commons Attribution 3.0 Unported Licence.

Introduction

Schiff bases are compounds with an azomethine (imine) group, synthesized for the first time 130 years ago by the German scientist Hugo Schiff. These compounds have been extremely well-studied by numerous research groups due to their excellent biological[1,2] and physicochemical properties.[3,4] Schiff bases are also excellent and diverse multidentate ligands that can be easily synthesized by a simple condensation reaction of an aldehyde or ketone with a primary amine. Such a simple synthetic procedure can also be used for the preparation of macrocyclic imine compounds with potential application in the extraction of metal[5,6] cations, anions,[7,8] and gaseous species.[9,10] Quinazolinones are a class of nitrogen heterocycles containing a fused benzene and pyrimidone ring in their structure and have immense pharmaceutical and biological potential.[11] Four groups of quinazolinones have been described in the literature, depending on the substitution pattern of the core structure: 2-substituted (**a**), 3-substituted (**b**), 2,3-disubstituted (**c**), and fused quinazolinones (**d**) (Scheme 1).[12,13]

Quinazolinone derivatives have been found in more than 200 natural alkaloids isolated from different plants and microorganisms.[12] Antibacterial,[14] antitumor,[15] anticonvulsant,[16] antidiabetic,[17] and antihypertensive[18] activities are among the most important biological properties displayed by quinazolinone derivatives. Furthermore, previous research has shown

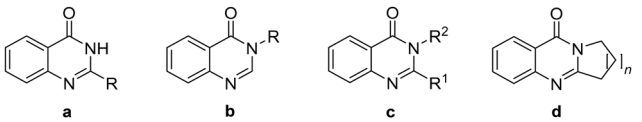

Scheme 1 The structure of substituted quinazolinones **a–d**.

[a] *Department of Chemistry, Josip Juraj Strossmayer University of Osijek, Cara Hadrijana 8/A, 31000 Osijek, Croatia. E-mail: tombalic@kemija.unios.hr*
[b] *Faculty of Food Technology Osijek, Josip Juraj Strossmayer University of Osijek, Croatia*
[c] *Department of Chemistry, Faculty of Science, Croatia University of Zagreb, Horvatovac 102a, HR-10000 Zagreb, Croatia*

† Electronic supplementary information (ESI) available. CCDC 2380330–2380334. For ESI and crystallographic data in CIF or other electronic format see DOI: https://doi.org/10.1039/d4nj04028g

Open Access Article. Published on 21 January 2025. Downloaded on 2/13/2026 11:23:58 AM. This article is licensed under a Creative Commons Attribution 3.0 Unported Licence.

that the quinazolinone core can also be used for the complexation of metal ions,[19] selective ratiometric fluorescence, visual detection of Fe(III) ions,[20] and positron emission tomography.[21] The first method for laboratory preparation of quinazolinones was described in 1869,[22] using anthranilic acid and cyanogen in ethanol. Over the past decades, many synthetic routes were developed for their preparation, including anthranilic acid and its derivatives,[23–25] isatoic anhydride,[26] substituted benzoxazinones,[27,28] and anilines as starting materials.[29,30] Such desirable properties of quinazolinones and Schiff's bases have resulted in the synthesis of a large number of quinazolinone Schiff base conjugates.[31,32] Recent research in this particular area has shown that quinazolinone Schiff base conjugates are potential inhibitors of SARS-CoV-2 proteins,[33,34] antioxidants,[35] anti-cancer agents,[36,37] and perspective chelating ligands for the preparation of structurally diverse coordination compounds.[38] The type and position of a substituent in imine or quinazoline compounds can readily be exploited in the design of specific properties. For example, in azomethine-linked aromatic Schiff bases, it was found that the substitution effect plays an important role in the reactivity profile of a compound.[39] A recent review of quinoline derivatives has indicated that these compounds can be rationally designed by changes in the substituent type and position for specific biological activity (*e.g.* viral resistance, antibacterial, and antimalarial).[40] The herein-described group of compounds was previously tested as dipeptidyl peptidase III inhibitors, and the OH-substituted compounds **2** and **3** have shown significant inhibitory activity (over 90%). In the molecular docking studies of these compounds, the authors identified the OH group in position 2 on the phenyl ring (Scheme 2 and Fig. S3 and S4, ESI†) as the most active in hydrogen bond formation with the enzyme active site, and that it made a significant contribution to the binding affinity.[41] As found in this investigation, this particular OH group tends to form intramolecular O–H···N hydrogen bonds with adjacent imine nitrogen atoms (*vide infra*) that can be important for positioning a compound in the enzyme active site[42] and for compound–enzyme hydrogen bond interactions. Such seemingly unimportant interaction can be an important piece of information, especially for theoretical (docking) investigations, emphasizing the importance of structural investigations (*i.e.* crystal structure determination). Although it is quite obvious that these compounds have enormous potential in many different fields, there is a surprisingly small number of investigations dealing with their solid-state structure. Only eight relevant structures were found in the CSD database.[43]

The above-mentioned properties of these compounds and the lack of structural investigations led us to study the molecular and crystal structure of four quinazoline-Schiff base conjugates (**1**, **2**, **3**, and **4**). Compounds were prepared according to previously reported procedures,[44] and single crystals were obtained using different solvents. Crystallization of **3** from methanol resulted in the formation of a methanol solvate (**3·MeOH**). The molecular and crystal structures were determined by single-crystal X-ray diffraction. The thermal properties of the compounds were investigated by TG/DSC methods. Intermolecular interactions were further studied by Hirshfeld surface analysis. Interaction and lattice energies were calculated and correlated with thermal properties.

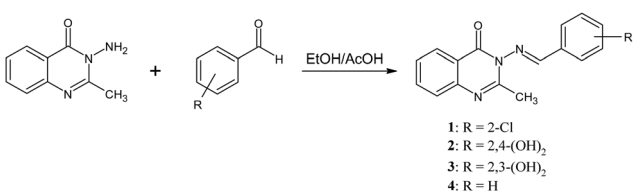

Scheme 2 Synthesis of quinazolinone Schiff bases.

Experimental

Reagents and techniques

All commercially available chemicals were of reagent grade. IR spectra were recorded on a Shimadzu FTIR 8400S spectrophotometer using a DRS 8000 attachment, in the 4000–400 cm^{-1} region. Thermogravimetric analyses were performed using a simultaneous TGA-DSC analyzer (Mettler-Toledo TGA/DSC 1). The samples (approx. 20 to 30 mg) were placed in aluminum pans (100 μL) and heated under a nitrogen atmosphere (200 mL min^{-1}) up to 400 °C at a rate of 5 °C min^{-1}. Before the measurements, a blank curve measurement was run under the same experimental conditions and then subtracted from the collected data. Data collection and analysis were performed using the program package STAR^e Software 10.0.[45]

Synthesis and crystallization

The quinazolinone Schiff bases **1–4** were prepared as described in our previous paper using a green chemistry methodology (Scheme 2).[44] Microwave-assisted synthesis was performed using a Milestone flexiWAVE reactor (Milestones Srl, Milan, Italy). Single crystals of compounds were obtained by recrystallization from appropriate organic solvents.

Synthesis of 3-{(*E*)-[(2-chlorophenyl)methylidene]amino}-2-methylquinazolin-4(3*H*)-one (1). A mixture of 3-amino-2-methylquinazolin-4(3*H*)-one (1.7 mmol; 0.3 g), 2-chlorobenzaldehyde (1.7 mmol; 192 μL) and glacial acetic acid (20 μL) in ethanol (10 mL) was stirred at 120 °C and 800 W for 30 min. The reaction mixture was cooled to room temperature, poured over crushed ice, and the crude product was collected by filtration.

Synthesis of 3-{(*E*)-[(2,4-dihydroxyphenyl)methylidene]amino}-2-methylquinazolin-4(3*H*)-one (2). A mixture of 3-amino-2-methylquinazolin-4(3*H*)-one (1.7 mmol; 0.3 g), 2,4-dihydroxybenzaldehyde (1.7 mmol; 235 mg) and glacial acetic acid (20 μL) in ethanol (10 mL) was stirred at 120 °C and 800 W for 30 min. The reaction mixture was cooled to room temperature, poured over crushed ice, and the crude product was collected by filtration.

Synthesis of 3-{(*E*)-[(2,3-dihydroxyphenyl)methylidene]amino}-2-methylquinazolin-4(3*H*)-one (3). A mixture of 3-amino-2-methylquinazolin-4(3*H*)-one (1.7 mmol; 0.3 g), 2,3-dihydroxybenzaldehyde (1.7 mmol; 235 mg) and glacial acetic acid (20 μL) in ethanol (10 mL) was stirred at 120 °C and 800 W for 30 min. The reaction mixture was cooled to room temperature, poured

 This journal is © The Royal Society of Chemistry and the Centre National de la Recherche Scientifique 2025

Open Access Article. Published on 21 January 2025. Downloaded on 2/13/2026 11:23:58 AM. This article is licensed under a Creative Commons Attribution 3.0 Unported Licence.

over crushed ice, and the crude product was collected by filtration.

Synthesis of (3-[(*E*)-benzylideneamino]-2-methylquinazolin-4(3*H*)-one (4). A mixture of 3-amino-2-methylquinazolin-4(3*H*)-one (1.7 mmol; 0.3 g), benzaldehyde (1.7 mmol; 173 μL) and glacial acetic acid (20 μL) in ethanol (10 mL) was stirred at 120 °C and 800 W for 30 min. The reaction mixture was cooled to room temperature, poured over crushed ice, and the crude product was collected by filtration.

X-Ray crystallography

Single-crystal X-ray diffraction data were collected at 295 K on an XtaLAB Synergy, Dualflex, HyPix diffractometer with graphite-monochromated Mo-Kα radiation (λ = 0.71073 Å) using ω-scans. Data reduction was performed using CrysAlis Pro.[46] Structures were solved using SHELXT and SHELXS programs[47,48] and refined using a full-matrix least-squares procedure based on F^2 using SHELXL[49] in the WINGX program suite.[50] All non-hydrogen atoms were refined anisotropically and hydrogen atoms in the structures were placed in calculated positions and refined using the riding model. The molecular structures of compounds and their molecular packing projections were prepared by Mercury.[51] Crystallographic data are summarized in Table 1.

Interaction energy calculation

The PixelC[52] program implemented in the Oscail software package[53] was used to calculate the interaction energies and crystal lattice energies. Cif files for the lattice energy and intermolecular energy calculations were prepared according to the requirements of PixelC and Oscail software. Calculations were done using Orca[54] and MultiWFN[55] using the WB97X-D3 computational model.[56]

Results and discussion

Crystal structures

Major differences both in the molecular and crystal structure of compounds were observed depending on the type of substituents on the benzene ring. The same is true for numerous intermolecular interactions in compounds, from strong O–H···N to weak C–H···O hydrogen bonds. The studied compounds are non-planar molecules, meaning that the dihedral angle between the quinazolinone and benzene moieties deviates from 0°. These deviations are also clearly visible in the N–N–C–C torsion angle values (an example is given in the ESI,† Fig. S1). The bond lengths and angles in all compounds are typical for both imines[57] and quinazolinones.[58] The values of bond lengths, angles, and torsion angles for all compounds can be found in the ESI† (Table S1), and basic crystallographic data are listed in Table 1.

The molecular structure of **1** is shown in Fig. S2 (ESI†). In this compound, two symmetrically independent molecules (A and B molecules in Fig. S2, ESI†) are present in the asymmetric unit of the compound. The difference between the two molecules is in the dihedral angles of the benzene and quinazolinone rings, as well as in the way they participate in hydrogen bonding. In molecule A, the dihedral angle is 23.83(10)°,

Table 1 Crystallographic data and structure refinement details for all compounds

Compound	**1**	**2**	**3**	**3·MeOH**	**4**
CCDC number	2380331	2380333	2380330	2380334	2380332
Empirical formula	$C_{16}H_{12}N_3OCl$	$C_{16}H_{13}N_3O_3$	$C_{16}H_{13}N_3O_3$	$C_{17}H_{17}N_3O_4$	$C_{16}H_{13}N_3O$
M_r	297.74	295.29	295.29	327.33	263.29
T/K	294.99(12)	294.98(11)	169.99(10)	294.98(11)	294.98(13)
Crystal system	Triclinic	Monoclinic	Monoclinic	Monoclinic	Monoclinic
Space group	$P\bar{1}$	$P2_1/n$	$P2_1/n$	$P2_1/n$	$P2_1/c$
a/Å	7.9879(3)	3.93860(10)	8.0290(3)	8.7501(10)	11.4544(6)
b/Å	13.1032(4)	29.5669(7)	12.7021(4)	8.9510(7)	15.8163(8)
c/Å	14.7678(6)	11.7999(2)	13.0187(4)	21.2255(13)	7.4627(4)
α/°	71.525(3)	90	90	90	90
β/°	76.046(3)	96.592(2)	93.446(3)	97.446(8)	103.569(6)
γ/°	81.964(3)	90	90	90	90
V/Å^3	1419.40(10)	1365.04(5)	1325.31(8)	1648.4(3)	1314.25(12)
Z	4	4	4	4	4
ρ_{calc}/g cm^{-3}	1.393	1.437	1.480	1.319	1.331
μ/mm^{-1}	0.271	0.843	0.105	0.096	0.086
F (000)	616.0	616.0	616.0	688.0	552.0
Crystal size/mm^3	0.27 × 0.2 × 0.09	0.24 × 0.04 × 0.03	0.58 × 0.41 × 0.24	0.48 × 0.12 × 0.09	0.63 × 0.08 × 0.05
Radiation	MoKα (λ = 0.71073)	CuKα (λ = 1.54184)	MoKα (λ = 0.71073)	MoKα (λ = 0.71073)	MoKα (λ = 0.71073)
2Θ range for data collection/°	5.268 to 50	5.978 to 134.892	4.484 to 59.966	5.976 to 49.984	6.178 to 49.98
Index ranges	$-9 \le h \le 9$, $-15 \le k \le 15$, $-17 \le l \le 17$	$-3 \le h \le 4$, $-33 \le k \le 35$, $-13 \le l \le 14$	$-11 \le h \le 11$, $-17 \le k \le 17$, $-18 \le l \le 18$	$-10 \le h \le 10$, $-10 \le k \le 10$, $-25 \le l \le 25$	$-13 \le h \le 13$, $-18 \le k \le 18$, $-8 \le l \le 8$
Reflections collected	22 130	10 228	16 812	14 101	17 675
Independent reflections	5005	2459	3868	2904	2312
Restraints/parameters	0/381	0/202	0/202	0/231	0/182
Goodness-of-fit on F^2	1.039	1.066	1.062	1.024	1.047
$R[F^2 > 4\sigma(F^2)]$	0.0477	0.0442	0.0409	0.0652	0.0564
w$R(F^2)$	0.1321	0.1275	0.1104	0.1633	0.1072
Largest diff. peak/hole/e Å^{-3}	0.34/−0.37	0.209/−0.216	0.38/−0.22	0.25/−0.27	0.13/−0.21

Open Access Article. Published on 21 January 2025. Downloaded on 2/13/2026 11:23:58 AM.
This article is licensed under a Creative Commons Attribution 3.0 Unported Licence.

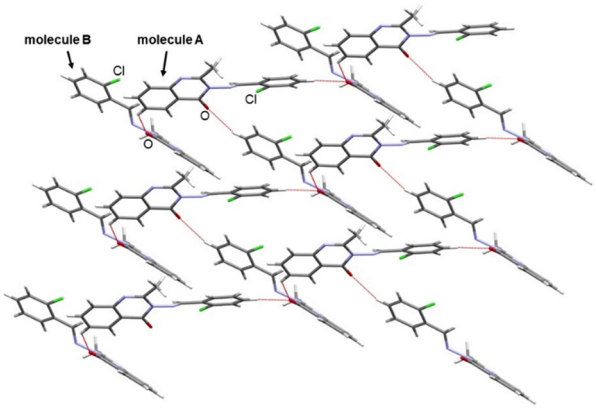

Fig. 1 Part of the crystal structure of **1** showing a fragment of the hydrogen bonded 2D layer spreading along the *a* and *b* crystallographic axes. View along the *c* crystallographic axis.

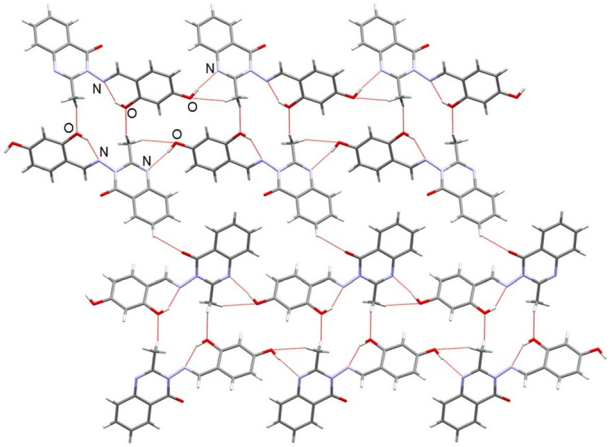

Fig. 2 Part of the crystal structure of **2** showcasing hydrogen bonding in a 2D layer. View along the *a* crystallographic axis. The layers are connected into a 3D network by additional C–H···O hydrogen bonds.

and in molecule B, it is 36.34(11)°. The molecules are connected *via* C–H···O hydrogen bonds into a 2D layer (d(C5–H5···O2) = 3.379 Å, ∠(C5–H5···O2) = 130.4°; d(C14–H14···O2) = 3.318 Å, ∠(C14–H14···O2) = 161.0°; d(C30–H30···O1) = 3.390 Å, ∠(C30–H30···O1) = 155.3°), with molecule A participating in two hydrogen bonds as a donor and its carbonyl oxygen atom an acceptor of one hydrogen bond, while molecule B participates in one hydrogen bond as a donor, and its carbonyl oxygen atom is a bifurcated hydrogen bond acceptor (Fig. 1 and Table S2, ESI†).

The molecular structure of **2** is shown in Fig. S3 (ESI†). In this compound, the 2,4-hydroxy substituted benzene moiety is connected to the quinazolinone moiety. Due to the vicinity of one of the –OH groups to the imine bond, a strong O–H···N intramolecular hydrogen bond is formed (Fig. S3, ESI†). The dihedral angle between quinazoline and benzene aromatic systems is 56.52(8)°. In the crystal, the molecules are connected by O–H···N hydrogen bonds (d(O3–H3···N1) = 2.857 Å, and ∠(O3–H3···N1) = 164.5°), thus forming infinite chains along the *c* axis. Adjacent chains are connected by a series of C–H···O hydrogen bonds (d(C5–H5···O1) = 3.228 Å, ∠(C5–H5···O1) = 130.0°; d(C9–H9C···O2) = 3.421 Å, ∠(C9–H9C···O2) = 163.9°) along the *b* axis (Fig. 2 and Table S2, ESI†), with the final 3D arrangement a result of additional C–H···O interactions along the *a* axis (d(C10–H10···O1) = 3.276 Å, ∠(C10–H10···O1) = 143.9°).

The molecular structure of **3** is shown in Fig. S4 (ESI†). The compound contains a 2,3-hydroxy substituted benzene moiety. As in the previous 2,4-substituted structure, a strong O–H···N intramolecular hydrogen bond is also present (Fig. S4, ESI†). Unlike in previous structures, the molecule of this compound is planar with a dihedral angle of 6.31(4)°. Such a flattening is not observed in **2** (dihedral angle of 56.52(8)°), despite the intramolecular O–H···N interaction. The reason for this can be found in the position of the –OH group nearest to the participating one (positions 3 and 4 in compounds **3** and **2**, respectively). The intermolecular interactions of this second –OH group (*e.g.* the O3–H3···N1 hydrogen bond) in **2** and the substantial rotational freedom of the benzene moiety along the C–C bond support the twisting of the benzene ring out of the quinazolinone ring plane. Consequently, the "locking" of the benzene moiety in the plane of the quinazoline moiety (or *vice versa*) decreases the number of favorable intermolecular interactions (especially those involving the –OH group). The final result of this effect is the lowering of electrostatic interaction energy (E_{ele}) and melting point (vide infra). In the crystal structure of **3**, the molecules are connected into infinite chains through O–H···N hydrogen bonds (d(O3–H3···N1) = 2.812 Å, ∠(O3–H3···N1) = 150.0°) along the *b* crystallographic axis that involve the –OH group and the nitrogen atom of the quinazolinone ring (Fig. 3). The chains are then connected into 3D by C–H···O hydrogen bonds (d(C7–H7···O1) = 3.376 Å, ∠(C7–H7···O1) = 157.7°; d(C9–H9B···O1) = 3.325 Å, ∠(C9–H9B···O1) = 140.0°).

The molecular structure of **3·MeOH** is shown in Fig. S5 (ESI†). The methanol molecule is bound *via* strong O–H···O hydrogen bonds to the hydroxybenzene system (Fig. 4). The dihedral angle between the two aromatic systems is 64.55(13)°. Interestingly, there are no intramolecular hydrogen bonds between –OH and imine nitrogen like in **2** and **3**. The reason for this is the insertion of a methanol molecule that acts as a better hydrogen bond acceptor than an imine nitrogen atom.

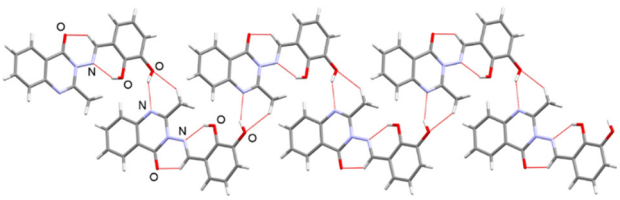

Fig. 3 Chains formed by O–H···N hydrogen bonds in part of the crystal structure of **3**, with additional supramolecular C–H···O interactions inside the chain and intramolecular O–H···N and C–H···O interactions. View along the *c* crystallographic axis. The chains are connected into a 3D network by C–H···O hydrogen bonds.

 This journal is © The Royal Society of Chemistry and the Centre National de la Recherche Scientifique 2025

Open Access Article. Published on 21 January 2025. Downloaded on 2/13/2026 11:23:58 AM.
This article is licensed under a Creative Commons Attribution 3.0 Unported Licence.

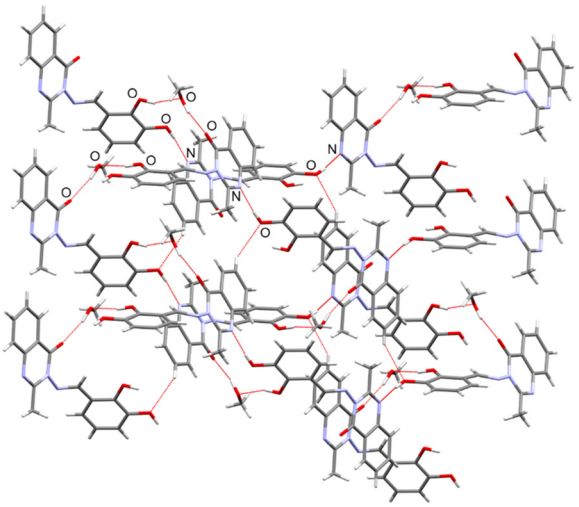

Fig. 4 Part of a 2D layer formed by O–H···O and O–H···N hydrogen bonding in **3·MeOH**. View along the *a* crystallographic axis. The layers are connected into a 3D network by C–H···O hydrogen bonding.

In the crystal, the molecules are primarily connected into infinite chains through O–H···N hydrogen bonds (d(O3–H2O···N1) = 2.720 Å, ∠(O3–H3···N1) = 174°) along the *c* crystallographic axis that involve the benzene moiety –OH group that is distant to the C=N bond, and the nitrogen atom of the quinazolinone ring. The neighboring chains are interconnected along the *a*-axis by O–H···O hydrogen bonds (d(O2–H1O···O4) = 2.680 Å, ∠(O2–H1O···O4) = 151°; d(O4–H3O···O1) = 2.786 Å, ∠(O4–H3O···O1) = 165°) between the –OH groups and methanol molecules into a layer. Layers are then connected into a 3D network through C–H···O hydrogen bonding (d(C9–H9B···O1) = 3.404 Å, ∠(C9–H9B···O1) = 143°).

In **4**, the quinazolinone moiety is connected to an unsubstituted benzene ring. The molecular structure is shown in Fig. S6 (ESI†). As in the previously described structures, the molecule is not planar, with a dihedral angle of 64.13(12)° between aromatic moieties. In this compound, molecules are connected into a 2D layer by a combination of an $R_2^2(10)$ hydrogen bonding motif, featuring two C–H···O hydrogen bonds with quinolinone carbonyl oxygen atoms (d(C4–H4···O1) = 3.341 Å, ∠(C4–H4···O1) = 139.7°), and orthogonal C–H···O interactions (d(C10–H10C···O1) = 3.396 Å, ∠(C10–H10C···O1) = 133.8°) between the quinolinone methyl groups and quinolinone carbonyl oxygen atoms (Fig. 5).

Hirshfeld surface analysis

Hirshfeld surface analysis (HSA) of the quinazolinone Schiff bases in the crystal structures was performed in CrystalExplorer 17.5,[57] and the results are shown in Fig. 6. The results show that H···H contacts, corresponding to some of the dispersive intermolecular interactions, form the largest part of the surface area, and their amount drops from 46% in unsubstituted **4**, through 41–43% in dihydroxy derivatives **2**, **3** and **3·MeOH**, to 38% in Cl-substituted **1**. This is naturally followed by an increase in the amount of H···O contacts from 10% in **4** to

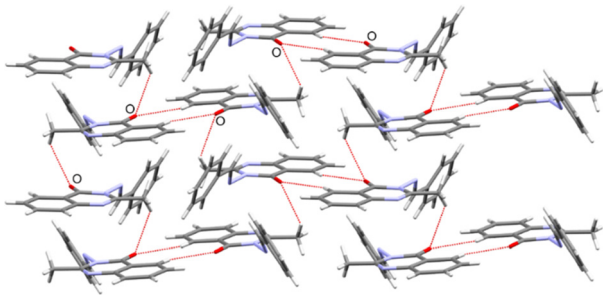

Fig. 5 Part of a 2D layer formed by C–H···O hydrogen bonding in **4**. View along the *a* crystallographic axis.

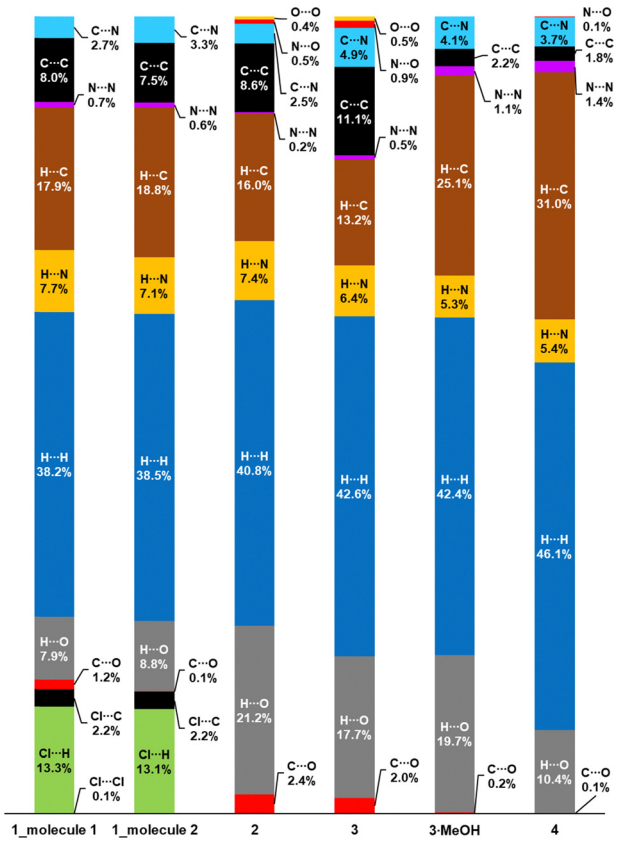

Fig. 6 Percentages of Hirshfeld surface areas corresponding to specified atom···atom contacts for quinazolinone molecules.

21%, 18%, and 20% in dihydroxy derivatives (**2**, **3**, and **3·MeOH**, respectively), as a result of the prominent hydrogen bonding motifs present therein. In **1** there is a drop to 8% due to the introduction of H···Cl contacts (13% of the surface area). The amount of H···N contacts mostly stays the same across the series, ranging from 8% in **1** to 5% in **4**. Most significantly, the amount of C···C contacts, which would correspond to π stacking interactions was found to be the lowest in unsubstituted **4** at only 2%, and higher in nonsolvated compounds **1**, **2**, and **3**, at 8%, 9%, and 11%, respectively. These observations are in accord with the results obtained by mapping the shape index to the obtained Hirshfeld surfaces (see Fig. S7, ESI†).

Open Access Article. Published on 21 January 2025. Downloaded on 2/13/2026 11:23:58 AM.
This article is licensed under a Creative Commons Attribution 3.0 Unported Licence.

Alternating approximately triangular or diamondoid red and blue areas on these maps, generally located on the quinazolinone fragment of the molecule, indicate π stacking interactions[59,60] and correspond to C···C contact areas of the Hirshfeld surfaces. In **1**, only one of the symmetry inequivalent Schiff base molecules participates in infinite π stacking *via* the quinazolinone fragment, with alternating shorter and longer intercentroid distances of 3.60 and 3.74 Å. The shorter distance corresponds to molecular pairs that stack both quinazolinone rings, while the longer one is for pairs that stack only one ring. The other symmetry inequivalent Schiff base molecules feature stack in pairs (in addition to stronger intermolecular interactions described above), with a longer intercentroid distance of 3.91 Å. In **2**, Schiff base molecules are infinitely π stacked *via* both the quinazolinone and aldehyde fragments, with an equal intercentroid distance of 3.94 Å. In **3**, since Schiff base molecules are rotated by 180° in each π stacked layer, each quinazolinone ring participates in stacking interactions with one adjacent aldehyde fragment ring, while each aldehyde fragment ring participates in stacking interactions with two quinazolinone rings. Like in the crystal structure of **1**, intercentroid distances alternate between 3.64 and 3.62 Å. The shorter distances between pairs are likely the result of the fact that data for this crystal structure was collected at 170 K instead of room temperature.

Thermal analysis (TG/DSC) and intermolecular interactions

TG/DSC curves of all compounds are given in the ESI† (Fig. S8–S11), DSC curves are presented in Fig. 7, and thermodynamic data for DSC measurements are given in Table S3 (ESI†). The thermal behavior of all compounds is rather similar – melting followed by single-step thermal decomposition. There are two distinct endothermic peaks in the DSC curve of **1**. These two events can be interpreted as melting points of two polymorphic forms – low melting form **I** and high melting form **II**. The PXRD diffractogram of the bulk material (Fig. S12, ESI†) confirms the presence of two distinct phases in the sample. The melting point of **I** is 148 °C (ΔH_{fus} = 8.15 kJ mol^{-1}; ΔS_{fus} = 0.019 kJ mol^{-1} K^{-1}) and 159 °C (ΔH_{fus} = 14.8 kJ mol^{-1}; ΔS_{fus} = 0.034 kJ mol^{-1} K^{-1}) for **II**. To determine the relationship between these two forms a linear Gibbs free energy diagram was constructed according to a previously published method (Fig. S13, ESI†).[61,62] According to Burger–Ramberger's heat of fusion, the entropy of fusion rules,[63] and the Gibbs energy diagram, the relationship between the two polymorphs is monotropic. 2,4-OH-substituted compound **2** has the highest melting point (226 °C, ΔH_{fus} = 27.43 kJ mol^{-1}), and Cl-substituted **1** has the lowest (148 °C and 159 °C). 2,3-OH-substituted **3** and unsubstituted **4** have melting points of 201 °C (ΔH_{fus} = 27.31 kJ mol^{-1}) and 192 °C (ΔH_{fus} = 26.31 kJ mol^{-1}), respectively.

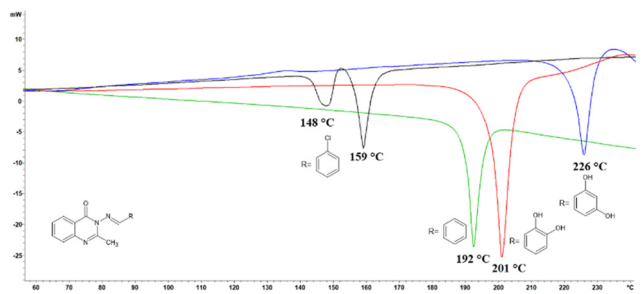

Fig. 7 DSC curves of **1** (black), **2** (blue), **3** (red) and **4** (green).

Intermolecular interaction and lattice energies were calculated to rationalize the influence of different substituents on melting points. The results of the calculations are summarized and presented in Table 2. Likewise, energies of the above-described hydrogen bond interactions were calculated using indicative lattice analysis (Table 3).[53] The calculated total interaction energies can be divided into discrete energy contributions. Coulomb or electrostatic interactions (E_{ele}) are due to hydrogen bond interactions, while dispersive (E_{dis}) energies can be attributed to aromatic interactions (*e.g.* π stacking), weak C–H···C interactions, and H···H contacts.[64] The individual contributions of specific energies to the total attractive energy ($E_{attractive}$) indicate that the largest contribution to crystal stability comes from dispersive interactions. As expected, the largest contribution of the dispersive component to lattice energy is from the unsubstituted compound **4** (67.7%). Most of the electrostatic contribution to the lattice energy in **4** is from weak C–H···O interactions involved in the formation of a 2D layered structure (C4–H4···O1 and C10–H10C···O1, energies of −8.24 kJ mol^{-1} and −8.48 kJ mol^{-1}, respectively). These interactions correspond to H···O contacts found by HSA analysis (approximately 10% contribution to the Hirshfeld surface). As calculated by the HSA analysis most of the crystal stabilization energy in this compound comes from dispersive H···C and H···H

Table 2 Intermolecular interaction energies (electrostatic (E_{ele}), polarization (E_{pol}), dispersion (E_{dis}), and repulsion (E_{rep}) in kJ mol^{-1}) for all compounds, and the sum of attractive interactions ($E_{attractive}$). The percentage contribution of individual attractive interaction energies to total energies is given in brackets

Compound/substituent on the benzene ring	E_{ele}	E_{pol}	E_{dis}	$E_{attractive}$	E_{rep}	PixelC	CLP	Melting point/°C
2/2,4-OH	−96.5 (30.1%)	−46.2 (14.4%)	−176.9 (55.3%)	−319.6	142.3	−177.3	−181.7	226
3/2,3-OH	−86.3 (27.2%)	−39.8 (12.5%)	−190.4 (60.0%)	−316.5	160.9	−155.6	−175.5	201
4/none	−55.9 (23.2%)	−23.5 (9.7%)	−160.9 (66.9%)	−240.3	93.3	−147.0	−153.8	192
1/Cl	−30.4 (12.1%)	−61.7 (24.6%)	−158.3 (63.2%)	−250.4	85.2	−165.2	−145.3	159[a]
3·MeOH/2,3-OH	−94.9 (40.1%)	−42.8 (18.1%)	−98.8 (41.7%)	−236.5	113.6	−122.7	−117.5	

[a] Value for higher melting point form II.

 This journal is © The Royal Society of Chemistry and the Centre National de la Recherche Scientifique 2025

Open Access Article. Published on 21 January 2025. Downloaded on 2/13/2026 11:23:58 AM. This article is licensed under a Creative Commons Attribution 3.0 Unported Licence.

Table 3 Selected hydrogen bond energies calculated using indicative lattice analysis for all compounds

Compound/substituent on the benzene ring	Interactions	d(D···A), ∠(D–H···A)	Symmetry	Energy (kJ mol^{-1})
1	C14–H14···O2	3.318(3), 161	$-x, 2-y, 1-z$	−12.41
	C5–H5···O2	3.379(3), 157	$1-x, 1-y, 1-z$	−8.20
	C30–H30···O1	3.390(3), 155	$1-x, 2-y, 1-z$	−10.80
2	O3–H3···N1	2.8567(17), 165	$x, y, 1+z$	−18.66
	C5–H5···O1	3.228(2), 130.0	$-1/2+x, 1/2-y, -1/2+z$	−9.84
	C9–H9C···O2	3.421(1), 164	$1-x, 1-y, 1-z$	−11.01
	C10–H10···O1	3.276(1), 144	$1+x, y, z$	−11.17
3	O3–H3···N1	2.8124(1), 150	$3/2-x, -1/2+y, 1/2-z$	−18.10
	C7–H7···O1	3.376(1), 158	$-1/2+x, 3/2-y, -1/2+z$	−11.23
	C9–H9B···O1	3.325(1), 139	$1-x, 1-y, 1-z$	−10.01
3·MeOH	O3–H2O···N1	2.720(3), 174	$1/2+x, 3/2-y, 1/2+z$	−24.06
	O2–H1O···O4	2.680(3), 151	x, y, z	−22.75
	O4–H3O···O1	2.786(3), 165	$1/2-x, 1/2+y, 3/2-z$	−21.08
4	C4–H4···O1	3.341(3), 140	$1-x, 1-y, 1-z$	−8.24
	C10–H10C···O1	3.396(4), 134	$x, 3/2-y, -1/2+z$	−8.48

contacts (77%), which agrees well with the value of dispersive contribution (67.7%, Table 2). The 2D layered motif in **1** is also built from weak C–H···O interactions involving carbonyl atoms of **A** and **B** molecules. In this case, these intralayer interactions are somewhat stronger (C14–H14···O2, C5–H5···O2 and C30–H30···O1, with energies of −12.41 kJ mol^{-1}, −8.20 kJ mol^{-1}, and −10.80 kJ mol^{-1}) in comparison with **4**. Other contributions to crystal stability are from dispersive H···C and H···H contacts, and to some extent from Cl···H contacts. The presence of Cl···H contacts increases the percentage of the polarization energy (E_{pol}) component (24.6%) in overall lattice energy, indicating the significant contribution of these interactions to overall crystal stability. Both compounds display similar packing motifs: 2D layers formed by weak C–H···O intralayer interactions connected to adjacent layers by weak dispersive interactions (Fig. 8). Although intralayer interactions are stronger in **1**, the melting point is lower by 40 °C compared to **4**. It is rational to presume that this occurs due to weaker interlayer interactions in **4**.

The highest contribution of electrostatic energy to the lattice energy is in **2**. This is due to several hydrogen bond interactions: O3–H3···N1 (−18.66 kJ mol^{-1}), C9–H9C···O2 (−11.01 kJ mol^{-1}) (Fig. 8), C10–H10···O1 (−11.17 kJ mol^{-1}), and C5–H5···O1 (−9.84 kJ mol^{-1}). Unlike in **1** and **4**, these electrostatic interactions are formed along all three crystallographic directions. These interactions are crucial for the overall lattice energy and melting point, as indicated by the H···O contribution to HS (21.2% – Fig. 6) and the percentage contribution of E_{ele} to total energy (30.1%). In **3**, the strongest intermolecular interaction is the O3–H3···N1 hydrogen bond (−18.10 kJ mol^{-1}) forming a chain-like motif. As discussed previously, the benzene ring in this molecule is co-planar with the quinazoline system, and the OH group in position 2 forms only intramolecular O–H···N interactions. Such a molecular configuration results in the formation of relatively strong electrostatic interactions in two crystallographic directions only (Fig. 9). The same corresponds to a lower percentage of H···O contacts found by HSA analysis (21.2% and 17.7% in **2** and **3**, respectively), lower lattice energy and the melting point of compound **3**.

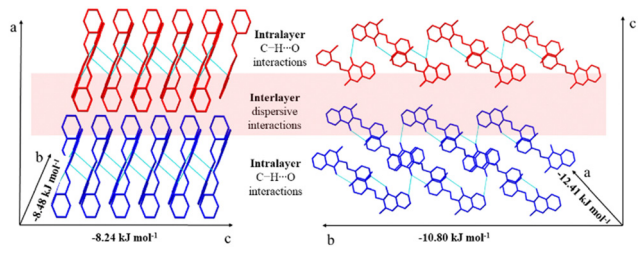

Fig. 8 Representation of major intralayer C–H···O interactions (light blue lines) with corresponding energies along the crystallographic axis in **4** (left) and **1** (right). Blue and red molecules are part of discrete layers. Hydrogen atoms are omitted for clarity.

Surprisingly, hydrogen bond interactions in **3·MeOH** display a substantial increase in hydrogen bond energies compared to those described above (Table 3). Most of these electrostatic interactions are realized between **3** (host) and methanol (guest) molecules, except for O3–H2O···N1 (−24.06 kJ mol^{-1}) which forms an infinite chain-like motif. These strong electrostatic interactions should result in an overall energy increase, but just the opposite is observed for **3·MeOH** (lowest lattice and attractive energies among those investigated). Some recent investigations[65,66] have shown that solvent insertion increases lattice energy, especially in porous materials. There are two plausible explanations for lattice energy decrease in **3·MeOH**: firstly, the calculated crystal density (1.319 g cm^{-3}) is lower than non-solvated compounds, implying an increase in intermolecular distances and weaker intermolecular interactions between host molecules. This can also be related to the Kitaigorodsky density rule (higher crystal density = higher lattice stability). Secondly, there is a significant decrease in dispersive interaction energy in **3·MeOH** (41.7%), which can be related to the energy of inter-host interactions. Although electrostatic interactions represent a major contribution to the

Open Access Article. Published on 21 January 2025. Downloaded on 2/13/2026 11:23:58 AM.
This article is licensed under a Creative Commons Attribution 3.0 Unported Licence.

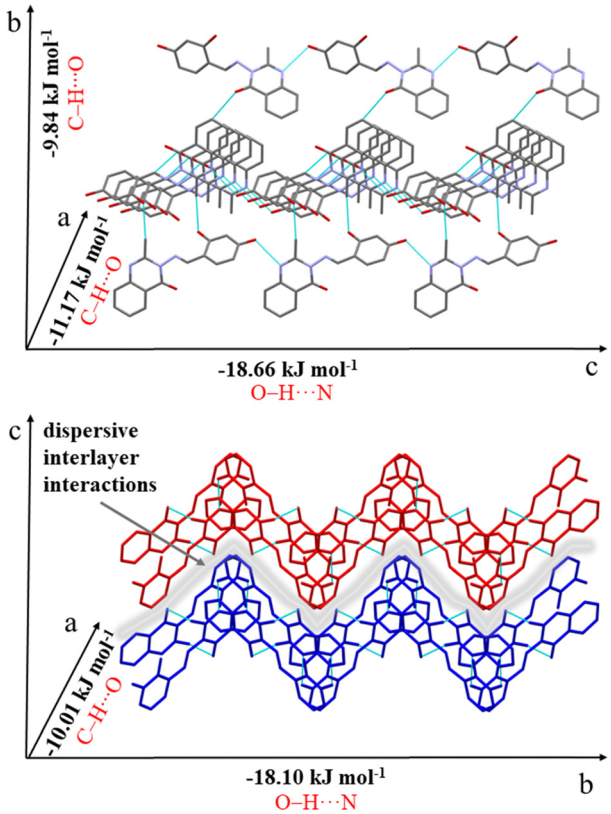

Fig. 9 Representation of major C–H···O and O–H···N interactions (light blue lines) with corresponding energies along the crystallographic axis in **2** (top) and **3** (bottom). Blue and red molecules are parts of discrete layers. Hydrogen atoms are omitted for clarity.

overall stability of a crystal, it is evident that in the case of solvent inclusion in an already dense packed structure (like **3**), these strong interactions impair overall stability by distancing host molecules. The unsubstituted compound (**4**) can be used as a starting point for further discussion regarding intermolecular interactions. In that case, substituents on benzene rings can be considered as elements that improve or impair crystal stability. It is quite obvious that strong hydrogen bond donors or acceptors (OH groups) increase crystal stability, while weak hydrogen bond acceptors (such as Cl) decrease stability, except in the case of the solvate. Although Cl (or any other halide substituent) can form intermolecular interactions it can be considered a steric hindrance for the formation of attractive dispersion interactions. Therefore, such substituents impair crystal stability not only because of their poor ability to form strong intermolecular interactions (''interactions effect'') but also due to the ''volume effect'' that inhibits the formation of attractive dispersion interactions. Obviously, in these compounds, there is a subtle interplay between the positive and negative impact of substituents that affects both crystal stability and consequently melting point.

To further investigate the influence of substituents on intermolecular interactions a Cambridge Structural Database (CSD)[39] search was performed and resulted in two relevant crystal structures (Fig. S14, ESI†): 2-OH, 5-Br – substituted compound (CSD code BEVPUQ)[58] and 2,5-methoxy substituted compound (CSD code SUMHOA).[67] The reported melting points of compounds are 121 °C (BEVPUQ) and 151 °C (SUMHOA), indicating weaker intermolecular interactions in these compounds than that reported herein. The lower melting point of the 2-OH–5-Br-substituted compound could be the halide substituent (as in **1**) and crystal water. The **3·MeOH** compound is also an example of the negative impact of the solvent on crystal stability (lowest calculated lattice energy). The melting point of the methoxy substituted compound (SUMHOA) is close to that of **1** (Cl substituted). Because the volume of the methoxy group is larger than chlorine, this indicates that crystal stability is predominantly governed by the type of potential hydrogen bond donor and acceptor, and the ''volume effect'' is of minor importance in these structures (there are two bulky methoxy groups in SUMHOA). Also, the position of the methoxy groups is such that it disfavors the formation of strong methoxy–methoxy interactions. Calculated values of lattice energy (PixelC and CLP in Table 2) agree very well with melting point values. A minor discrepancy is the PixelC value for **1** which is unreasonably high compared to higher melting point compounds. The CLP lattice energy calculation however is the lowest for this compound. It is interesting to note that the melting point correlates with the percentage contributions of dispersive and electrostatic interactions – higher values of electrostatic interactions and lower values of dispersive interactions are characteristic of high melting point compounds and exactly the opposite was observed for compounds with a lower melting point (Fig. 10). This observation correlates with the percentage of H···O contacts found by HSA analysis and energy of major electrostatic interactions calculated by indicative lattice analysis (*vide supra*).

From the above considerations, useful conclusions for crystal engineering of thermally stable organic compounds can be stated: (i) the primary source of crystal stability comes from strong electrostatic interactions due to the ''interaction effect''. The same can be observed from HSA analysis, which shows a

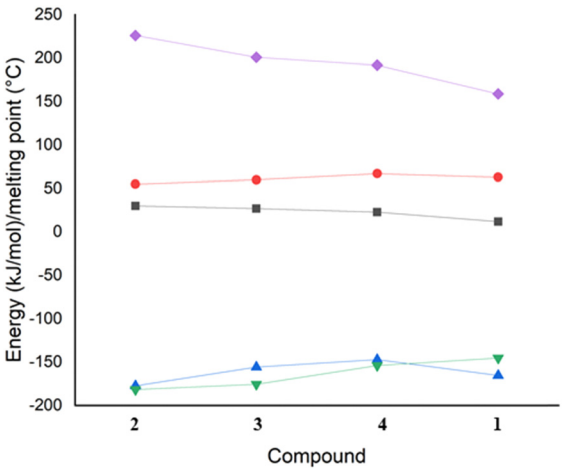

Fig. 10 Correlation of melting points (violet), E_{dis} (red), lattice energies (PixelC – blue), lattice energies (CLP – green), and E_{ele} (brown). E_{dis} and E_{ele} are given as percentage contributions.

 This journal is © The Royal Society of Chemistry and the Centre National de la Recherche Scientifique 2025

Open Access Article. Published on 21 January 2025. Downloaded on 2/13/2026 11:23:58 AM. This article is licensed under a Creative Commons Attribution 3.0 Unported Licence.

higher proportion of H···O contacts in compounds with higher melting points (**2** and **3**). (ii) Dispersive interactions are important for stability, but easily sterically hindered. For example, the proportion of C···C contacts (which can be considered as an indicator of π-stacking interactions) found by HSA analysis is smaller in the solvate compound (**3·MeOH**) and the Cl-substituted compound (**1**). (iii) Weak hydrogen bond acceptors (such as Cl) cause a decrease in crystal stability. The presence of such substituents leads to an increased number of contacts in which they participate (percentage of H···Cl contacts in HSA analysis), but these interactions are weak, resulting in a decrease in crystal stability and ultimately a lower melting point. (iv) The presence of solvent molecules within this group of compounds increases the percentage of electrostatic interaction energies, but decreases the crystal density, resulting in weaker host–host interactions and lower crystal stability.

IR spectroscopy

IR spectra of all compounds can be found in the ESI† (Fig. S15–S18). The spectra are similar, with the most pronounced differences from 3600 to 2400 cm^{-1}, due to the vibrations of substituent groups on the benzene ring. Vibrations close to 1670 cm^{-1} can be assigned to C=O stretching vibrations (1684 cm^{-1}, 1678 cm^{-1}, 1672 cm^{-1}, and 1670 cm^{-1} in **1**, **3**, **2**, and **4**, respectively). Noticeably, this vibration is slightly shifted towards lower wave numbers in **3**, **2**, and **4** due to the involvement of this group in C–N···O hydrogen bond interactions (*vide supra*). Strong vibrations close to 1610 cm^{-1} can be assigned to C=N stretching vibrations of the imine group. Similar results of FT-IR were previously observed for Br-substituted quinazoline analogs.[58]

Conclusions

The compounds reported herein represent rare examples of structurally characterized quinazolinone Schiff base conjugates. Specifically, these compounds can be described as Schiff bases composed of a 2-methyl-quinazoline-4-one moiety and a substituted benzene moiety connected by the imine bond. In terms of the molecular structure, the compounds exhibit similarities, with the most pronounced differences being observed in the dihedral angle between the quinazolinone and benzene moieties. OH-substituted compounds (**2** and **3**) primarily form strong O–H···N hydrogen bonds in the crystal state. The unsubstituted (**4**) and Cl-substituted (**1**) compounds form N–H···O hydrogen bonds and weak N–H···O and C–H···O hydrogen bond interactions. Thermal analysis reveals that OH-substituted compounds exhibit the highest melting points (226 °C and 201 °C for **2** and **3**, respectively), while unsubstituted and Cl-substituted compounds display somewhat lower melting points. Intermolecular interaction calculations and HSA analysis have shown that higher values of electrostatic interactions and lower values of dispersive interactions are characteristic of high melting point compounds and exactly the opposite was observed for compounds with a lower melting point, except in the solvate compound (**3·MeOH**). Therefore, it can be concluded that the primary source of crystal stability comes from electrostatic interactions (strong hydrogen bonds), and weak hydrogen bond acceptors (such as Cl) cause a decrease in overall crystal stability in comparison to unsubstituted and OH-substituted compounds. The results presented here are important not only for the crystal engineering of thermostable organic compounds but also provide information for theoretical calculations, such as docking studies.

Author contributions

Milenko Korica: data curation, investigation, and formal analysis. Maja Molnar: data curation and writing – reviewing and editing. Mario Komar: formal analysis, investigation, and writing – original draft preparation. Vinko Nemec: formal analysis, investigation, writing – original draft preparation, and writing – reviewing and editing. Dominik Cinčić: formal analysis, investigation, writing – original draft preparation, and writing – reviewing and editing. Tomislav Balić: conceptualization, methodology, writing – original draft preparation, data curation, writing – reviewing and editing, and formal analysis.

Data availability

The data supporting this article have been included within the manuscript and its ESI.†

Conflicts of interest

There are no conflicts to declare.

Acknowledgements

This work has been supported in part by the Croatian Science Foundation under the project "Green Technologies in Synthesis of Heterocyclic Compounds" (UIP-2017-05-6593).

Notes and references

1 C. M. da Silva, D. L. da Silva, L. V. Modolo, R. B. Alves, M. A. de Resende, C. V. B. Martins and Â. de Fátima, *J. Adv. Res.*, 2011, **2**, 1–8.
2 P. Przybylski, A. Huczynski, K. Pyta, B. Brzezinski and F. Bartl, *Curr. Org. Chem.*, 2009, **13**, 124–148.
3 J. L. Segura, M. J. Mancheño and F. Zamora, *Chem. Soc. Rev.*, 2016, **45**, 5635–5671.
4 K. C. Gupta and A. K. Sutar, *Coord. Chem. Rev.*, 2008, **252**, 1420–1450.
5 W. Al Zoubi, *J. Coord. Chem.*, 2013, **66**, 2264–2289.
6 T. Balić, B. Matasović, B. Marković, A. Šter, M. Štivojević and D. Matković-Čalogović, *J. Inclusion Phenom. Macrocyclic Chem.*, 2016, **85**, 217–226.
7 A. Sap, B. Tabakci and A. Yilmaz, *Tetrahedron*, 2012, **68**, 8739–8745.

Open Access Article. Published on 21 January 2025. Downloaded on 2/13/2026 11:23:58 AM. This article is licensed under a Creative Commons Attribution 3.0 Unported Licence.

8 M. K. Deliomeroglu, V. M. Lynch and J. L. Sessler, *Supramol. Chem.*, 2017, **30**, 807–821.
9 M. Korica, I. Balić, L. M. van Wyk, D. P. van Heerden, V. I. Nikolayenko, L. J. Barbour, T. Jednačak, I. Đilović and T. Balić, *Microporous Mesoporous Mater.*, 2022, **332**, 111708.
10 T. Balić, B. Marković, J. Jaźwiński and D. Matković-Čalogović, *Microporous Mesoporous Mater.*, 2016, **226**, 53–60.
11 M. Asif, *J. Chem.*, 2014, **2014**, 1–16.
12 U. A. Kshirsagar, *Org. Biomol. Chem.*, 2015, **13**, 9336–9352.
13 M. Demeunynck and I. Baussanne, *Curr. Med. Chem.*, 2013, **20**, 794–814.
14 M. A. Sayyed, S. S. Mokle and Y. B. Vibhute, *ARKIVOC*, 2006, **2006**, 221–226.
15 W. M. El-Husseiny, M. A.-A. El-Sayed, A. S. El-Azab, N. A. AlSaif, M. M. Alanazi and A. A.-M. Abdel-Aziz, *J. Enzyme Inhib. Med. Chem.*, 2020, **35**, 744–758.
16 A. S. El-Azab and K. E. H. ElTahir, *Bioorg. Med. Chem. Lett.*, 2012, **22**, 1879–1885.
17 M. S. Malamas and J. Millen, *J. Med. Chem.*, 1991, **34**, 1492–1503.
18 I. Khan, S. Zaib, S. Batool, N. Abbas, Z. Ashraf, J. Iqbal and A. Saeed, *Bioorg. Med. Chem.*, 2016, **24**, 2361–2381.
19 W. Cao, X.-J. Zheng, D.-C. Fang and L.-P. Jin, *Dalton Trans.*, 2015, **44**, 5191–5196.
20 P. R. Dongare, A. H. Gore, U. R. Kondekar, G. B. Kolekar and B. D. Ajalkar, *Inorg. Nano-Met. Chem.*, 2017, **48**, 49–56.
21 J. Hou, M. S. Kovacs, S. Dhanvantari and L. G. Luyt, *J. Med. Chem.*, 2018, **61**, 1261–1275.
22 P. Griess, *Ber. Dtsch. Chem. Ges.*, 1869, **2**, 415–418.
23 M. Komar, M. Molnar and A. Konjarević, *Croat. Chem. Acta*, 2020, **92**, 511–517.
24 M. Baghbanzadeh, M. Molnar, M. Damm, C. Reidlinger, M. Dabiri and C. O. Kappe, *J. Comb. Chem.*, 2009, **11**, 676–684.
25 M. Adib, S. Ansari, A. Mohammadi and H. R. Bijanzadeh, *Tetrahedron Lett.*, 2010, **51**, 30–32.
26 S. Y. Abbas, K. A. M. El-Bayouki, W. M. Basyouni and E. A. Mostafa, *Med. Chem. Res.*, 2017, **27**, 571–582.
27 M. Komar, M. Molnar, M. Jukić, L. Glavaš-Obrovac and T. Opačak-Bernardi, *Green Chem. Lett. Rev.*, 2020, **13**, 93–101.
28 Y. A. Ammar, Y. A. Mohamed, A. M. El-Sharief, M. S. A. El-Gaby and S. Y. Abbas, *Chem. Sci. J.*, 2011, **2**, CSJ-15.
29 Z. Zheng and H. Alper, *Org. Lett.*, 2008, **10**, 829–832.
30 L. He, H. Li, H. Neumann, M. Beller and X. Wu, *Angew. Chem., Int. Ed.*, 2013, **53**, 1420–1424.
31 E. Bagheri, K. Saremi, F. Hajiaghaalipour, F. L. Faraj, H. M. Ali, M. A. Abdulla, S. L. Khaing and N. Salehen, *Curr. Pharm. Des.*, 2018, **24**, 1395–1404.
32 S. S. Kazemi, A. Keivanloo, H. Nasr-Isfahani and A. H. Amin, *J. Heterocycl. Chem.*, 2018, **55**, 1651–1657.
33 M. A. Mansour, A. M. AboulMagd and H. M. Abdel-Rahman, *RSC Adv.*, 2020, **10**, 34033–34045.
34 J. Liu, Y. Liu, J. Jian and X. Bao, *Chin. J. Org. Chem.*, 2013, **33**, 370.
35 Z. Hricovíniová, M. Hricovíni and K. Kozics, *Chem. Pap.*, 2017, **72**, 1041–1053.
36 K. P. Rakesh, H. M. Manukumar and D. C. Gowda, *Bioorg. Med. Chem. Lett.*, 2015, **25**, 1072–1077.
37 M. Zahedifard, F. Lafta Faraj, M. Paydar, C. Yeng Looi, M. Hajrezaei, M. Hasanpourghadi, B. Kamalidehghan, N. Abdul Majid, H. Mohd Ali and M. Ameen Abdulla, *Sci. Rep.*, 2015, **5**, 1–17.
38 F. Khajoee Nejad, M. Khosravan, S. Y. Ebrahimipour and F. Bisceglie, *Appl. Organomet. Chem.*, 2017, **32**(1), 1–9.
39 N. Kumar, A. Khanna, K. Kaur, H. Kaur, A. Sharma and P. M. S. Bedi, *Mol. Diversity*, 2022, **27**, 1905–1934.
40 A. Khurshid, A. Saeed, M. F. Erben, T. Hökelek and E. Jabeen, *J. Mol. Struct.*, 2023, **1273**, 134215.
41 D. Agić, M. Karnaš, S. Tomić, M. Komar, Z. Karačić, V. Rastija, D. Bešlo, D. Šubarić and M. Molnar, *J. Biomol. Struct. Dyn.*, 2022, **41**, 7567–7581.
42 B. M. Hudson, E. Nguyen and D. J. Tantillo, *Org. Biomol. Chem.*, 2016, **14**, 3975–3980.
43 C. R. Groom, I. J. Bruno, M. P. Lightfoot and S. C. Ward, *Acta Crystallogr.*, 2016, **B72**, 171–179.
44 M. Komar, F. Prašnikar, T. G. Kraljević, K. Aladić and M. Molnar, *Curr. Green Chem.*, 2021, **8**, 62–69.
45 STARe, Software 10.0, 2009, Mettler-Toledo GmbH.
46 Oxford Diffraction, Oxford Difraction Ltd., Xcalibur CCD system, CRYSALIS Software system, Version 1.171.34.44, 2010.
47 G. M. Sheldrick, *Acta Crystallogr., Sect. A:Found. Adv.*, 2015, **71**, 3–8.
48 G. M. Sheldrick, *Acta Crystallogr., Sect. A:Found. Crystallogr.*, 2008, **64**, 112–122.
49 G. M. Sheldrick, *Acta Crystallogr., Sect. A:Found. Adv.*, 2015, **71**, 3–8.
50 L. J. Farrugia, *J. Appl. Crystallogr.*, 2012, **45**, 849–854.
51 C. F. Macrae, I. J. Bruno, J. A. Chisholm, P. R. Edgington, P. McCabe, E. Pidcock, L. Rodriguez-Monge, R. Taylor, J. van de Streek and P. A. Wood, *J. Appl. Crystallogr.*, 2008, **41**, 466–470.
52 A. Gavezzotti, *Z. Kristallogr. – Cryst. Mater.*, 2005, **220**, 499–510.
53 P. McArdle, *J. Appl. Crystallogr.*, 2017, **50**, 320–326.
54 F. Neese, *Comput. Mol. Sci.*, 2017, **8**, e1327.
55 T. Lu and F. Chen, *J. Comput. Chem.*, 2011, **33**, 580–592.
56 J.-D. Chai and M. Head-Gordon, *Phys. Chem. Chem. Phys.*, 2008, **10**, 6615.
57 A. Blagus, D. Cinčić, T. Friščić, B. Kaitner and V. Stilinović, *Maced. J. Chem. Chem. Eng.*, 2010, **29**, 117.
58 S. Y. Ebrahimipour, M. Khosravan, J. Castro, F. Khajoee Nejad, M. Dusek and V. Eigner, *Polyhedron*, 2018, **146**, 73–80.
59 A. Saeed, S. Ashraf, U. Flörke, Z. Y. Delgado Espinoza, M. F. Erben and H. Pérez, *J. Mol. Struct.*, 2016, **1111**, 76–83.
60 E. E. Salama, M. F. Youssef, A. T. A. Boraei, M. Haukka, S. M. Solima, A. Barakat and A. A. M. Sarhan, *Crystals*, 2023, **13**, 992.
61 E. Marti, *J. Therm. Anal.*, 1988, **33**, 37–45.
62 T. Balić, F. Perdih, M. Počkaj, M. Molnar, M. Komar and I. Balić, *J. Mol. Struct.*, 2021, **1231**, 129957.
63 A. Burger and R. Ramberger, *Mikrochim. Acta*, 1979, **72**, 273–316.
64 T. Balić, M. Paurević, M. Počkaj, M. Medvidović-Kosanović, D. Goman, A. Széchenyi, Z. Preisz and S. Kunsági-Máté, *Molecules*, 2022, **27**, 3781.

 This journal is © The Royal Society of Chemistry and the Centre National de la Recherche Scientifique 2025

65 T. Haj Hassani Sohi, F. Maass, C. Czekelius and V. Vasylyeva, *Crystals*, 2023, **13**, 1512.
66 D. P. McMahon, A. Stephenson, S. Y. Chong, M. A. Little, J. T. A. Jones, A. I. Cooper and G. M. Day, *Faraday Discuss.*, 2018, **211**, 383–399.
67 U. Panchsheela Ashok, S. Prasad Kollur, B. Prakash Arun, C. Sanjay, K. Shrikrishna Suresh, N. Anil, H. Vasant Baburao, D. Markad, J. Ortega Castro, J. Frau, N. Flores-Holguín and D. Glossman-Mitnik, *Inorg. Chim. Acta*, 2020, **511**, 119846.

Open Access Article. Published on 21 January 2025. Downloaded on 2/13/2026 11:23:58 AM.
This article is licensed under a Creative Commons Attribution 3.0 Unported Licence.